

Spectral & Timing analysis of Be/X-ray binary EXO 2030+375 during its giant 2021 outburst

Ruchi Tamang,¹★ Manoj Ghising,¹† Mohammed Tobrej,¹‡ Binay Rai,¹§
Bikash Chandra Paul¹¶

¹Department of Physics, North Bengal University, Siliguri, Darjeeling, WB, 734013, India

15 November 2022

ABSTRACT

We report the X-ray spectral and timing analysis of the high mass X-ray binary EXO 2030+375 during the 2021 type II outburst. We have incorporated NuSTAR, NICER, *Swift*/BAT & *Fermi*/GBM observations to carry out a comprehensive analysis of the source. Pulse profiles in different energy ranges and time intervals have been generated and analyzed. We have performed a brief comparison of the observations amidst the peak outburst condition and also during the decaying state of the outburst. Pulse profiles are found to evolve with time and energy. An iron emission line at (6–7) keV is observed in the X-ray continuum. Distinct absorption features were observed in the spectra corresponding to the peak outburst state while such features were not detected during the later decaying phase of the outburst. We have estimated the characteristic spin-up time scale to be ~ 60 years. The continuum flux of the system and the varying luminosities covering the entire outburst period have been used to interpret the characteristics of the source. We have summarized the variability of various parameters along with their underlying physical implications.

Key words: X-rays: binaries–star: neutron–accretion, accretion discs–pulsars: individual: EXO 2030+375

1 INTRODUCTION

EXO 2030+375 is a transient, accretion powered X-ray pulsar and is one of the member of the Be/X-ray binaries. Be/X-ray binaries are binary systems formed between a neutron star and a Be star. Neutron stars in Be/X-ray binaries (BeXRBs) revolve in a wide and moderate eccentric orbits (Tauris & Van Den Heuvel 2006). Strong X-ray outbursts are observed due to an instantaneous mass accretion from the circumstellar envelope onto the neutron star while passing close to the periastron. The intensity of such an outburst rises up to a certain level than the quiescent phase. Normally, BeXRBs undergo periodic (Type I) X-ray outbursts observed at the periastron passage of the neutron star. Such outbursts cover $<(20\text{--}30)\%$ of the orbit lasting for a few days to weeks (Stella, White & Rosner 1986). On the other hand, giant outbursts (Type II) are also observed from the neutron stars in BeXRBs. Such outbursts cover an integral fraction or multiple orbits and are normally known to last for several weeks to months (Okazaki & Negueruela 2001; Reig 2011; Jaisawal & Naik 2016; Wilson-Hodge *et al.* 2018; Jaisawal *et al.* 2019). Type II X-

ray outbursts are quite rare and hence very rarely detected. These are independent of the orbital phase or periastron passage of the binary. The X-ray activities in BeXRBs are characterized by the Type-I outbursts with peak luminosity of the order of $L_x \leq 10^{37} \text{ erg s}^{-1}$ and rare giant (Type-II) X-ray outbursts with peak luminosity of $L_x \geq 10^{37} \text{ erg s}^{-1}$. Depending upon the evolution of the donor, mass transfer from the companion star to the compact object occurs via capture of stellar wind or accretion from a large circumstellar disk around the companion star (Paul & Naik 2011). The optical companion of such systems is a non-supergiant B or O type star bearing emission lines in its spectrum (Reig 2011).

EXO 2030+375 is a well analyzed BeXRB associated with regular Type-I outbursts during almost every periastron passage. This transient accreting source was discovered in 1985 with EXOSAT during a Type-II outburst (Parmar *et al.* 1989) with ~ 42 s pulsations. The optical counter-part of EXO 2030+375 is a highly reddened B0 Ve star (Motch & Janot-Pascheco 1987) which shows infrared excess and H α in emission (Coe *et al.* 1988). Using the relation between extinction and distance of sources in the Galactic plane, Wilson *et al.* (2002) estimated the distance of EXO 2030+375 as 7.1 kpc. Type-I X-ray outbursts of EXO 2030+375, occurs almost at every periastron passage of its ~ 46 day orbit (Wilson *et al.* 2008) and have been monitored with the X-ray instruments onboard RXTE, INTEGRAL, XMM-Newton, Suzaku and *Swift*/BAT observatories. The characteristic properties of the source (Wilson *et al.*

★ ruchitamang76@gmail.com

† E-mail:manojghising26@gmail.com

‡ tabrez.md565@gmail.com

§ binayrai21@gmail.com

¶ bcpaul@nbu.ac.in

2002; Naik *et al.* 2013; Naik & Jaisawal 2015; Ferrigno *et al.* 2016; Epili *et al.* 2017), have been studied using the available observational data. In June 2006, EXO 2030+375 was observed to undergo a giant (Type-II) X-ray outburst for the second time with an initial flux of 180 mCrab. This value is higher than the previous peak flux of about 50 mCrab observed during the entire life of the RXTE/ASM mission (Corbet & Levine 2006). This outburst was also followed by *Swift*/BAT which reported that the peak flux increased to 750 mCrab (Krimm *et al.* 2006). Spin-up feature was reported in the source during the giant X-ray outbursts in 1985 (Parmar *et al.* 1989) and 2006 (Wilson *et al.* 2008) while spin-down episodes have been reported during low luminous outbursts in 1994–2002 (Wilson *et al.* 2002; Wilson, Fabregatet & Coburn 2005) and also during faint outbursts after March 2016 (Kretschmar *et al.* 2016). The spectra of EXO 2030+375 during outbursts after 2006 have been described using various phenomenological and physical models which showed an iron emission line at ~ 6.4 keV and interstellar absorption (Epili *et al.* (2017) and references therein). Various interesting features have been observed in the spectrum of the system.

Suzaku observations of EXO 2030+375 during Type-I outbursts in 2007 and 2012 did not reveal the presence of cyclotron absorption features in the X-ray spectrum. Presence of additional matter at certain pulse phases of the source was reported as the reason of prominent absorption dips in the pulse profiles (Naik *et al.* (2013); Naik & Jaisawal (2015)). During the brighter Type-I outburst in 2007, Naik *et al.* (2013) reported the detection of narrow emission lines (i.e Si XII, Si XIV, S XV) for the first time along with Fe K α and Fe XVI in the continuum spectrum. Detailed analysis of the source was carried out by using extensive RXTE pointed observations during many Type-I & 2006 Type-II outbursts starting from 1995 to 2011 (Epili *et al.* 2017). Timing and spectral analysis were carried out in (3–30) keV luminosity range from 3.8×10^{36} to $2.6 \times 10^{38} \text{ erg s}^{-1}$, covering the complete span of RXTE campaign. Temporal studies of more than 600 RXTE pointings verified the evolution of pulse profiles with luminosity. A major peak and a minor peak at low luminosity transformed to a dual peaked profile with minor dips at high luminosity. This signifies that pulse profiles at a particular luminosity were identical irrespective of the X-ray outbursts character which reveals that the emission geometry is mainly dependent upon the accretion rate. Since its discovery in 1985, the system has undergone X-ray outbursts regularly. Since 2015, the Type-I outbursts are found to possess diminishing intensity and eventually vanished from the light curve towards the end of 2015 or early 2016 (Fürst *et al.* 2016). Type-I X-ray outburst activity began in early 2016 proceeding with much fainter peak luminosity. Fürst *et al.* (2017) detected pulsation at a minimum luminosity of $6.8 \times 10^{35} \text{ erg s}^{-1}$ in (3–78) keV range, which is the lowest luminosity of the source with X-ray pulsations in the light curve. The pulsar was observed with *Swift*/XRT at a fainter phase and the data quality was found to be poor for pulsation search. Pulsations in the light curve at lower luminosity to that during the earlier *Swift*/XRT observation (Fürst *et al.* 2017), rules out the onset of propeller regime.

In this paper, we compare and reveal the characteristic features of EXO 2030+375 during the peak state and the decaying state of the outburst. The pulse period of the source is found to be $\sim 41.27 \pm 0.004$ s. An iron emission line at (6–7) keV is observed in the X-ray continuum. Absorption features are revealed in the spectrum corresponding to the peak outburst state while such features are not prominent in the decaying state (post -peak outburst state). Furthermore, several NICER observations have been taken into consideration to explore certain features of the source during the recent giant outburst. We have tried to present a comprehensive

study of the source using its temporal and spectral properties by interpreting the sequential variations of various parameters .

2 OBSERVATIONS AND DATA REDUCTION

The source EXO 2030+375 previously exhibited two giant Type II outbursts in 1985 and 2006. On July 2021, the source was reported to encounter another giant Type II outburst by MAXI/GSC observations. Constant monitoring of the source was carried out by Monitor of All-sky X-ray Image (MAXI), the Burst Alert Telescope (BAT) on the *Swift* satellite and Gamma-ray Burst Monitor (GBM) on the Fermi satellite. Throughout the bursting phase, NICER started observing the source regularly. For our analysis, we have considered observations from Neutron Star Interior Composition Explorer (NICER), Nuclear Spectroscopic Telescope Array (NuSTAR) along with some relevant observations from *Fermi*/GBM and *Swift*/BAT.

2.1 NUSTAR

The data reduction for EXO 2030+375 has been done using HEASOFT 6.29 and CALDB v 1.0.2. NuSTAR is sensitive in the (3–79) keV energy range and is the first hard X-ray focusing telescope. It consists of two independent co-aligned grazing incident telescopes which are similar but not identical. Each of the telescopes have their own focal plane module FPMA and FPMB consisting of a solid state CdZnTe detector (Harrison F. A *et al.* 2013). The light curves, spectra, response matrices and effective area files are generated using NUSTARDAS software v 0.4.9. The clean event files were filtered from the unfiltered event files using the mission specific command NUPIPELINE. A circular region of 100'' around the source center and away from the source has been taken into consideration as the required source and background regions respectively. The estimated source and background have been used for extracting light curves and their corresponding spectra by using the *ftool* XSELECT and imposing the mission specific command line NUPRODUCTS. For both FPMA and FPMB data, the backgrounds are individually subtracted and their light curves are combined using tool LCMATH . The two NuSTAR observations (80701320002 and 90701336002) have been considered for performing the required timing and spectral analysis of the system. The observation coined with observation ID 80701320002 coincides close to the peak outburst period of the source, while the other observation (90701336002) corresponds to the decaying phase of the giant outburst respectively. NuSTAR observation ID 80701320002 and 90701336002 are hereafter referred as Obs I and Obs II respectively.

The specifications related to the NuSTAR and NICER observations under consideration are presented in *table 1*.

2.2 NICER

NICER is an International Space Station (ISS) external payload (Gendreau *et al.* 2016) designed for the study of neutron stars through soft X-ray Timing. In our work, we have used X-ray Timing Instrument (XTI), which operates in the energy range of (0.2–12.0) keV. The standard data screening and reduction of NICER observations were carried out using NICERDAS v9 and CALDBv xti20210720. For each observations, the background estimation was done using the tool nibackgen3C50 v6 (Remillard *et al.* 2021). The clean event files were filtered using command NICERL2. The filtered event files were then loaded to XSELECT to extract the necessary source light curve & pha files. Response and arf files were

Observatory	Observation ID	Date of Observation (MJD)	Exposure (ks)	Observatory	Observation ID	Date of Observation (MJD)	Exposure (ks)
NuSTAR	80701320002	59456.0389	32.461	NICER	4201960101	59423.2131	2.114
	90701336002	59526.1466	23.487		4201960102	59431.008	1.335
NICER	4201960103	59435.0881	2.062		4201960103	59483.3313	2.549
	4201960104	59447.7555	0.614		4201960130	59485.3322	2.547
	4201960105	59448.8604	0.961		4201960131	59487.3361	2.449
	4201960106	59449.2481	1.323		4201960132	59489.3348	2.263
	4201960107	59450.8667	0.849		4201960133	59491.2719	2.64
	4201960108	59451.1829	7.815		4201960134	59493.0138	2.529
	4201960109	59452.0963	4.206		4201960135	59497.0168	2.805
	4201960110	59453.3183	3.889		4201960137	59526.1587	15.381
	4201960111	59454.4093	2.674		4201960150	59527.3846	3.249
	4201960112	59455.1194	2.496		4201960151	59529.6428	2.238
	4201960113	59456.5959	2.299		4201960152	59529.6428	2.238
	4201960115	59458.0882	2.483		4201960153	59530.4166	1.554
	4201960116	59459.1791	2.337		4201960154	59532.354	2.041
	4201960118	59463.1863	4.408		4201960156	59535.1945	2.778
	4201960119	59465.0039	2.601		4201960157	59536.2273	2.445
	4201960121	59466.9951	3.738		4201960158	59538.1635	1.951
					4201960159	59540.2461	0.418
					4201960162	59544.0572	2.372

Table 1. NuSTAR and NICER observations indicated by their observation IDs along with their respective date of observations and exposure.

generated using command NICERARF & NICERRMF. From the NICER clean event files, light curves in (0.7-10.0) keV energy range with a binning of 0.01s were extracted. The spectra in the energy range (0.7-10.0) keV has been considered for fitting. This is because there will be background domination above 10 keV and also the spectra below 0.7 keV has been ignored to get rid of the calibration issue. We have considered 37 NICER observations from July 28, 2021 to November 26, 2021 that lies during the outburst phase of EXO 2030+375 in 2021.

The necessary barycentric correction has been done for both NuSTAR and NICER observations to account for the orbit correction. The required spectral fitting has been carried out using XSPEC version 12.12.0 (Arnaud 1996).

2.3 Fermi/GBM

The Fermi Gamma-Ray Space Telescope studies the gamma-ray sources and was launched in 2008. It has a Gamma-ray Burst Monitor (GBM) which is efficient in the energy range 20 MeV to about 300 GeV (Meegan *et al.* 2009). We have considered the publicly available pulsar data for our analysis as it provides an estimate of the source flux in the hard band. The spin frequency provided by FERMI GBM Accreting Pulsars Program (GAPP) has been used to obtain the spin frequency derivative by linearly fitting three consecutive pulse frequencies (Serim *et al.* 2022). The rate of change of spin frequency is given by the slope of the plot and the error associated with it corresponds to 1-sigma uncertainty in measuring the spin-up rate.

2.4 Swift/BAT

Swift has been purposely designed to study the Gamma-ray burst. It has its monitoring instrument called the Burst Alert telescope which works in searching for transient events in the energy band of (15-50) keV from 80% of the sky (Barthelmy *et al.* 2005). The

daily light curves for EXO 2030 +375 has been used as an indicator of bolometric flux during the outburst which are available in the official website, the Hard X-rays Transient Monitor (Krimm *et al.* 2013).

3 TIMING ANALYSIS

3.1 NuSTAR

We generated the light curves corresponding to the NuSTAR data with the help of *ftool* LCMATH. The approximate pulse period of the source was roughly estimated by Fast Fourier Transform using the command POWSPEC. The tool EFSEARCH helps in determining the more accurate period by folding the light curve with large number of periods around the approximate period by Chi-Square maximization technique also known as the epoch-folding technique (Davies (1990); Larsson (1996)). Thus, the best pulse period was precisely estimated to be $\sim 41.2 \pm 0.004$ s. The uncertainty in the measurement of pulsation has been taken care by using method described in Boldin *et al.* (2013). The light curves are folded with the corresponding estimated pulse period to obtain the pulse profile using *ftool* EFOLD in the energy range of (3-79) keV. The pulse profile obtained is highly defined and displays a main pulse preceded by various intensity minima. We extracted the light curves with a binning of 0.01s. The entire energy band was resolved into various sub-intervals as (3-7) keV, (7-12) keV, (12-18) keV, (18-24) keV, (24-30) keV, (30-35) keV and (35-79) keV. Corresponding to each interval, the energy resolved pulse profiles were generated in order to analyze the dependency of the shape and amplitude of pulse profiles with energy as shown in figure 2.

The pulse profile was found to evolve with time and energy. This is supported by the luminosity-resolved pulse profiles presented in figure 5. The pulse profiles correspond to observations at different spans of time where the variability is significant. Also, the energy resolved pulse profiles presented in figure 2 reveals distinct

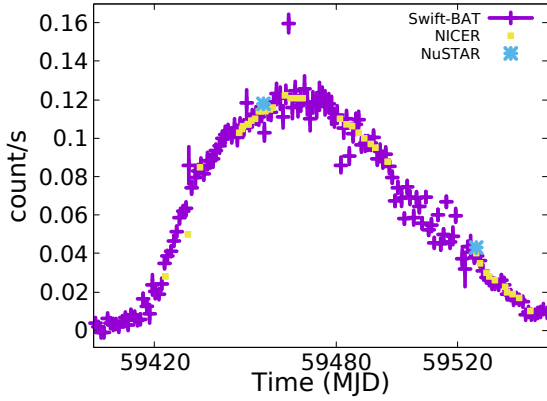


Figure 1. *Swift*/BAT (15-50) keV light curve of the source. The *Swift*/BAT, NICER and NuSTAR observations are marked in purple, yellow and blue respectively.

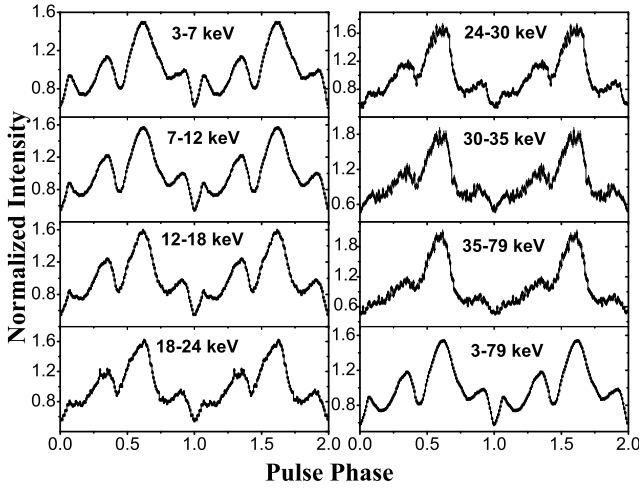


Figure 2. Energy Resolved pulse profiles corresponding to NuSTAR Obs I (59456 MJD) near the maximum of the outburst. Energy is expressed in keV.

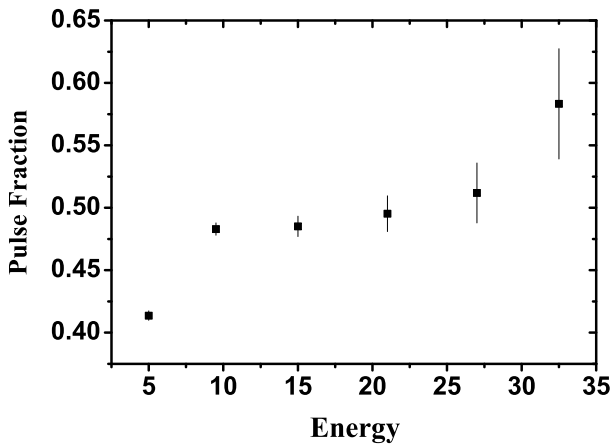


Figure 3. Pulse Fraction of the source with respect to energy (keV) using NuSTAR observation Id 80701320002. The errors quoted are within 3σ level uncertainty.

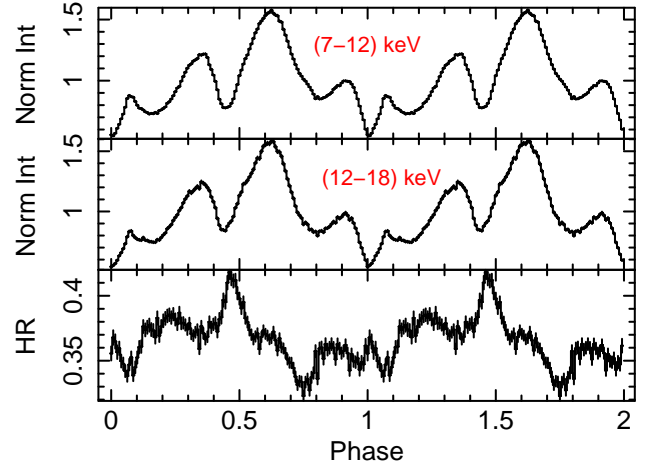


Figure 4. Variation of hardness ratio with pulse phase.

variabilities in the nature of the pulse profiles which characterizes the energy evolution of the pulse profiles. The variation is mostly significant in the pulse profile in the pulse phases between (0-0.2) and (0.8-1.0). As proposed by [Shaw et al. \(2009\)](#), the pulse profile which are multi peaked below 20 keV evolves to single peaked nature. This feature was relevantly observed in our observations as well. The major peak was found to be dominant with increasing energy which may reflect the transition in the accretion states. At higher energies, uncertainties are associated with the normalized count rates. The Pulse Fraction (P.F) parameter is defined as the ratio of the difference and sum of maximum P_{max} and minimum P_{min} intensities of pulse profile expressed as, $P.F = \frac{P_{max} - P_{min}}{P_{max} + P_{min}}$. The variation of the pulse fraction with energy has been shown in [figure 3](#). The pulse fraction increases with energy by $\sim 7\%$ in the (7-12) keV range up to $\sim 13.4\%$ in the (24-30) keV energy range.

We also examined the Hardness Ratio (HR) with respect to the pulse phase of the system. The hardness ratio (HR) in the (7-12 keV & 12-18 keV) energy band of NuSTAR observation has been illustrated in the [figure 4](#). The variations as observed in the HR shows spin phases where hard X-rays exceeds the soft X-rays between (0.4-0.5). Interestingly, the minima of HR lies between pulse phase \sim (0.7-0.8). Thus, we observed a phase shift in the minima of HR as compared to the minima of the pulse profile.

3.2 NICER

For timing analysis, we considered 37 NICER observations which revealed the evolution of pulse period with time and luminosity in the soft energy band. The NICER observations in the time span 59423 MJD to 59544 MJD have been taken into consideration. Corresponding to each observation, we estimated the approximate pulse period and hence obtained the best period. The light curves obtained were folded corresponding to the estimated best period to generate the pulse profiles. The pulse profiles have been observed to remarkably vary with luminosity. As the luminosity increases, the dominant X-ray beaming pattern is found to evolve from pencil-beam to a fan-beam nature on approaching close to maximum of the outburst ([Parmar et al. 1989](#)) with the main peak becoming more dominant as seen in the [figure 5](#).

The *Fermi*/GBM estimated data shows that the spin frequency has increased to ~ 24.27 mHz on 59536 MJD in (15-50) keV energy

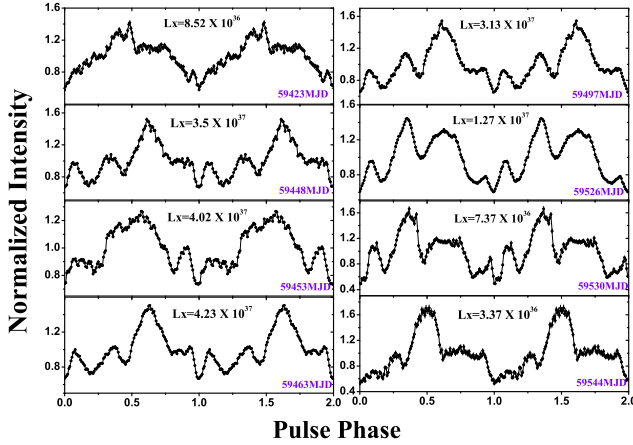


Figure 5. Luminosity (erg s^{-1}) resolved pulse profiles corresponding to NICER observations of EXO 2030+375. Luminosity dependence of the pulse profiles can be clearly seen. Two pulses in each panel are shown for clarity.

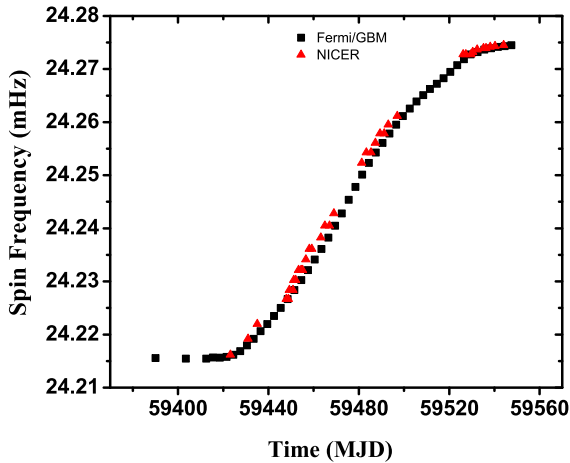


Figure 6. Evolution of spin frequency with time of EXO 2030+375 during 2021 outburst. Spin frequencies estimated by *Fermi*/GBM are marked in black whereas the red marks correspond to the spin frequencies obtained from NICER observations.

range. We plotted the *Fermi*/GBM estimated data along with the spin frequencies obtained from NICER observations as shown in *figure 6*. The *Swift*/BAT light curves of 2021 outburst along with the NICER and NuSTAR observations taken during different stages of the outburst have been presented alongside in *figure 1*. We obtained the bolometric flux by multiplying the observed *Swift*/BAT count rate by the conversion factor $A \sim 1.072 \times 10^{-7}$ (L., Ji *et al.* 2019). The corresponding luminosities were computed by considering a distance of 7.1 kpc (Wilson *et al.* 2002).

From the spin frequency data provided by *Fermi*/GBM, we estimated the spin frequency derivative. The variation of spin frequency derivative with respect to luminosity has been presented in *figure 7*. The frequency derivative bears a positive correlation with the luminosity of the system. The data points are well fitted using the POWER-LAW model which is in accordance with the accre-

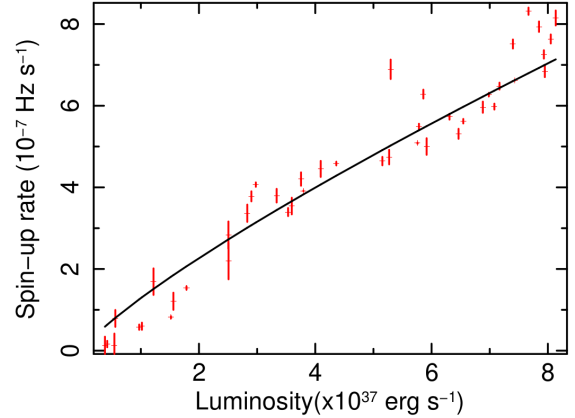


Figure 7. Variation of spin-up rate with the luminosity. The solid line represents the best fitted line by using POWER-LAW model.

tion torque model established by Ghosh & Lamb (1979) given by $\dot{\nu} \propto L^{6/7}$. We obtained the POWER-LAW index as 0.82 ± 0.004 .

As mentioned in the preceding section, the pulse period of the source is estimated to be $\sim 41.2 \pm 0.004$ s. Using the $\dot{\nu}$ vs luminosity plot, we estimated the pulse period derivative. The characteristic spin-up time scale ($-P/\dot{P}$) is found out to be ~ 60 years which is longer than those estimated during first ~ 30 years (Parmar *et al.* 1989) and second giant outburst ~ 40 years (Klochkov *et al.* 2007).

4 SPECTRAL ANALYSIS

As analyzed earlier by Naik *et al.* (2013), Ferrigno *et al.* (2016), the source EXO 2030+375 shows some complex absorption features in its spectrum and cannot be modeled using simple power-law/cutoff model. In the course of choosing the right model for fitting the spectrum, Wilson *et al.* (2008) used power-law/cutoff model modified with Gaussian absorption line at ~ 10 keV which they interpreted as the presence of cyclotron line. However, Klochkov *et al.* (2007) fitted the spectrum considering a broad emission “bump” at ~ 15 keV. For our analysis, we first considered the NuSTAR Obs I that falls around the maximum of the outburst for spectral fitting as shown in *figure 8*. The model combination of CONSTANT*PHABS*CUTOFFPL showed an emission like feature in the energy range (6-7) keV and the spectra was well fitted with the addition of GAUSSIAN model to it. This indicated the presence of He-like Fe line at ~ 6.6 keV. On using the continuum model combination CONSTANT*PHABS*(CUTOFFPL+GAUSSIAN), the spectrum showed a highly significant negative residuals at ~ 10 keV. We used different such model combinations to fit the broad band spectrum of the source. A CONSTANT model has been used in order to take into account for the instrumental uncertainties. Including GAUSSIAN absorption model (GABS) to the model combination and referring it as model I i.e., CONSTANT*PHABS*(CUTOFFPL+GAUSSIAN)*GABS fitted the spectrum well as it flattens the residuals showing GABS line at ~ 10.12 keV reducing chi square from 1.61 to 1.18. The model combination II i.e., CONSTANT*PHABS*(CUTOFFPL+GAUSSIAN+GAUSSIAN) considering broad emission feature at ~ 16 keV (Klochkov *et al.* 2007) resulted in a reduced chi square value as 1.28.

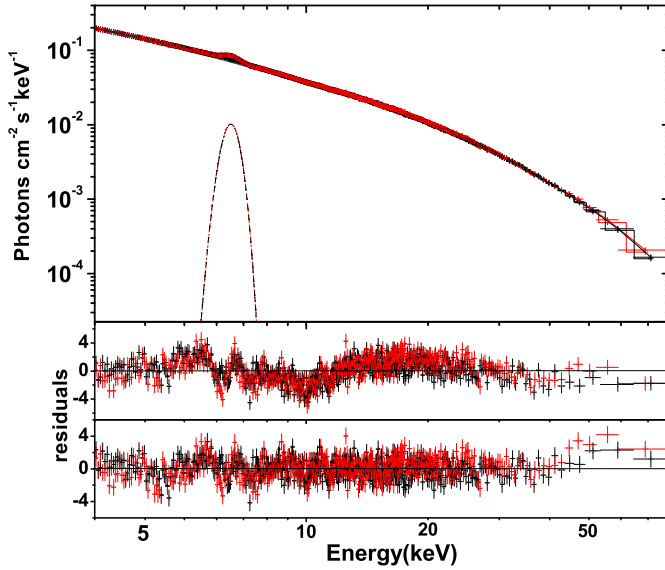


Figure 8. Broad band spectrum of EXO 2030+375 using NuSTAR observation. The top panel represents the unfolded spectrum. Negative residuals can be observed at ~ 10 keV as relevant from the middle panel. The bottom panel represents the best fitted spectra.

Wilson *et al.* (2008) and Klochkov *et al.* (2008) also successfully used HIGHECUT model to fit the source spectra. Thus, using the continuum model III i.e., CONSTANT*PHABS*(HIGHECUT*POWERLAW+GAUSSIAN)*GABS *GABS reduced chi square to 1.18. The spectrum is also fitted well incorporating the Fermi-Dirac cutoff power law (FDCUT) (Tanaka 1986) model into the model combination IV as CONSTANT*PHABS*(FDCUT+GAUSSIAN)*GABS reducing chi square value to 1.25 with GABS line energy at ~ 10.33 keV. We also tried spectral fitting including the Negative and Positive power law EXponential (NPEX) (Mihara 1995) model into the model combination V i.e., CONSTANT*PHABS*(NPEX+GAUSSIAN)*GABS which reduced chi square to 1.19 with GABS line energy at ~ 10.26 keV. While using NPEX model, we kept the positive index fixed at 2 whereas the negative index was allowed to freely vary. Amongst all of the model combinations we considered, model I and model III has been found to noticeably reduce chi square value by a significant amount as compared to the other model combinations. The fitted spectra has been shown in figure 8 and the corresponding statistical data has been presented in table 2. However, such features were not observed while fitting the spectrum of NuSTAR Obs II. This may be due to its comparatively low luminosity than the maximum of the outburst as it lies in the decaying phase of the outburst (59526 MJD). We calculated the flux in (3-79) keV energy range with the help of command flux in the terminal and thus calculated the corresponding luminosity to be $\sim 9.49 \times 10^{37} \text{ erg s}^{-1}$ and $\sim 3.41 \times 10^{37} \text{ erg s}^{-1}$ for Obs I and II respectively at a distance of 7.1 kpc.

For all the NICER observations taken under consideration for analysis, we obtained their respective fluxes and the corresponding luminosities. Observations made throughout the outburst, revealed the enhancement of the continuum flux from $1.41 \times 10^{-9} \text{ erg cm}^{-2} \text{ s}^{-1}$ on July 28, 2021 and reached

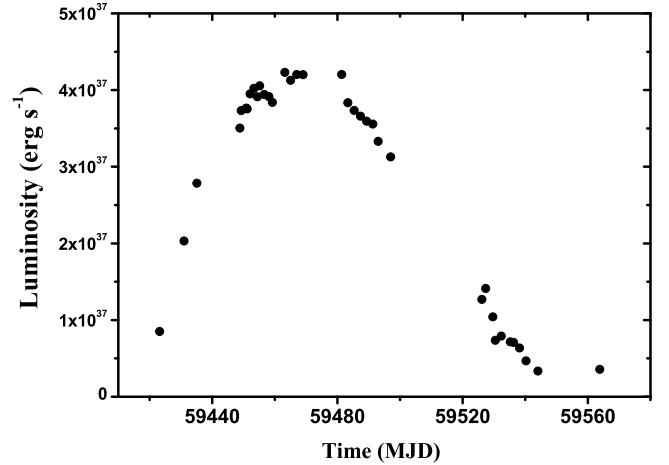


Figure 9. Variation of Luminosity (erg s^{-1}) with respect to time as obtained from NICER observations.

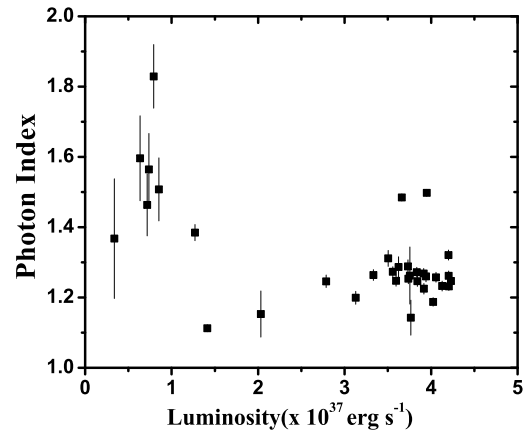


Figure 10. Variation of power-law photon index with 0.7-10.0 keV luminosity ($\times 10^{37} \text{ erg s}^{-1}$) are shown for NICER observations of EXO 2030+375. Luminosities are measured assuming the distance of the source as 7.1 kpc.

its maximum value of $7.02 \times 10^{-9} \text{ erg cm}^{-2} \text{ s}^{-1}$ on September 6th, 2021. After attaining its maximum value, the (0.7-10.0) keV flux gradually decreased with time to a minimum of $\sim 5.58 \times 10^{-10} \text{ erg cm}^{-2} \text{ s}^{-1}$ on around 59544 MJD. The variation of luminosity with respect to time has been shown in figure 9. It can be clearly seen that the maximum luminosity attained by the source is $\sim 4.23 \times 10^{37} \text{ erg s}^{-1}$ which gradually decreases to its minimum value of $\sim 3.37 \times 10^{36} \text{ erg s}^{-1}$ on 59544 MJD. The spectra have been fitted in the energy range of (0.7-10.0) keV using a single continuum model PHABS*(BBODY+POWERLAW). For the observations with luminosity of the order $\sim 10^{37} \text{ erg s}^{-1}$, we used an additional GAUSSIAN model to the continuum model. The emission like feature observed between (6-7) keV was well fitted by GAUSSIAN model reducing chi square from ~ 1.98 to 1.49 for a particular NICER observation. However, for the observations having luminosity $\leq 10^{37} \text{ erg s}^{-1}$, no such emission feature was observed.

From the spectral analysis of these NICER observations, we

Parameters	Model I	Model II	Model III	Model IV	Model V
n_H (cm^{-2})	0.42 ± 0.034	0.83 ± 0.044	0.99 ± 0.044	1 ± 0.031	0.61 ± 0.038
photon index	1.06 ± 0.003	1.19 ± 0.008	1.4 ± 0.007	1.29 ± 0.003	--
E_{cut} (keV)	17.6 ± 0.079	20.11 ± 0.184	12.57 ± 0.098	5(fixed)	78.51 ± 1.135
E_{fold} (keV)	--	--	20.76 ± 0.229	16.54 ± 0.057	--
E_{Fe} (keV)	6.51 ± 0.006	6.49 ± 0.006	6.51 ± 0.006	6.51 ± 0.006	6.51 ± 0.006
σ_{Fe} (keV)	0.29 ± 0.008	0.34 ± 0.007	0.3 ± 0.007	0.31 ± 0.007	0.29 ± 0.007
Ga (keV)	--	16.09 ± 0.558	--	--	--
Ga sigma (keV)	--	6.33 ± 0.429	--	--	--
E_{gabs_1} (keV)	10.12 ± 0.059	--	11.85 ± 0.148	10.33 ± 0.07	10.26 ± 0.06
E_{σ_1} (keV)	2.13 ± 0.092	--	2.68 ± 0.24	1.13 ± 0.08	1.96 ± 0.1
$Gabs_{strength_1}$	0.24 ± 0.014	--	0.82 ± 0.292	0.07 ± 0.006	0.19 ± 0.015
E_{gabs_2} (keV)	--	--	17.45 ± 2.638	--	--
E_{σ_2} (keV)	--	--	4.89 ± 1.769	--	--
$Gabs_{strength_2}$	--	--	0.68 ± 0.437	--	--
χ^2_ν	3272.05	3560.36	3265.59	3456.22	3311.17
d.o.f	2776	2776	2772	2776	2775
Reduced χ^2_ν	1.18	1.28	1.18	1.25	1.19

Table 2. Best-fit model parameters obtained from the spectral fitting of NuSTAR Obs I of EXO 2030+375 during 2021 outburst with Model I (CONSTANT*PHABS*(CUTOFFPL+GAUSSIAN)*GABS), Model II (CONSTANT*PHABS*(CUTOFFPL+GAUSSIAN+GAUSSIAN)), Model III (CONSTANT*PHABS*(HIGHECUT*POWERLAW+GAUSSIAN)*GABS*GABS), Model IV (CONSTANT*PHABS*(FDCUT+GAUSSIAN)*GABS) and Model V (CONSTANT*PHABS*(NPEX+GAUSSIAN)*GABS). The hydrogen column density n_H is of the order of $10^{22} cm^{-2}$. Errors are within 90% confidence interval. Ga in the table denotes the second GAUSSIAN MODEL used in the Model II.

observed the dependency of photon index with luminosity. Thus, we plotted the photon index for all the NICER observations along with the observed luminosity as shown in figure 10. A bi-modal behavior in the variation of the power-law index with increasing luminosity was observed. This observation validates the fact that the spectral shape depends on the rate of mass accretion. A negative correlation between the power-law photon index and luminosity signifies the pulsar spectrum to be relatively soft at lower luminosities. However, a positive correlation between power-law photon index and luminosity can be observed as luminosity approaches higher values. The pulse fraction shows negative correlation with luminosity as can be seen in figure 11.

5 PHASE RESOLVED SPECTROSCOPY

The phase resolved spectral analysis of the NuSTAR Obs Id 80701320002 was performed in order to understand the variation of different spectral parameters with the pulse phase. Firstly, we divided each pulse into ten equal intervals and their respective good time interval (GTI) files were created. These GTI files were then used for the generation of FPMA and FPMB spectras using the tool XSELECT. The spectras obtained for different phase intervals are fitted again with the same continuum model consisting of CONSTANT, PHABS, CUTOFFPL, GASUSSIAN and GABS. The flux and corresponding luminosities are calculated for each intervals. We observed that with the pulse phase, the corresponding flux value varies between $(1.54 - 1.57) \times 10^{-8} erg cm^{-2} s^{-1}$. The photon index value (α) and the highcut energy (E_{cut}) varies between (1.08-1.11) and (17.05-17.94) keV respectively. The value of Fe emission line initially decreases from 6.55 to 6.48 keV and then again suddenly increases from 6.52 to 6.54 keV between phase (0.5-0.8). However, an abrupt decrease in its value to 6.50 keV

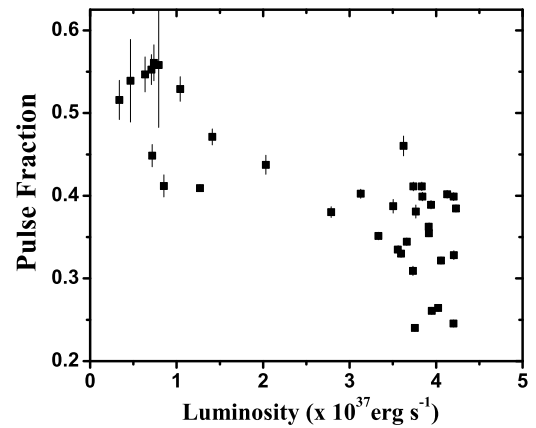


Figure 11. Variation of pulse fraction with luminosity in (0.7-10) keV energy range corresponding to NICER observations.

is observed between phase (0.8-0.9) after which again it gradually increases to its maximum of 6.55 keV. The maximum value of equivalent width of He like iron (σ_{Fe}) has been obtained at 0.38 keV which is observed between (0.4-0.5). The absorption feature E_{gabs} has its maximum at 10.27 keV in between interval (0-0.1) and then slightly decreases reaching a value of 8.4 keV in between (0.1-0.2). It again increases to 9.1 keV in between (0.3-0.4) followed by decrease in its value towards minimum at 7.98 keV between interval (0.8-0.9) and then rises again to 9.67 keV in (0.9-1.0) interval. The maximum value of σ_{gabs} is 4.53 keV which lies between phase interval (0.1-0.2). The gabs strength value varies between (0.23-0.92)

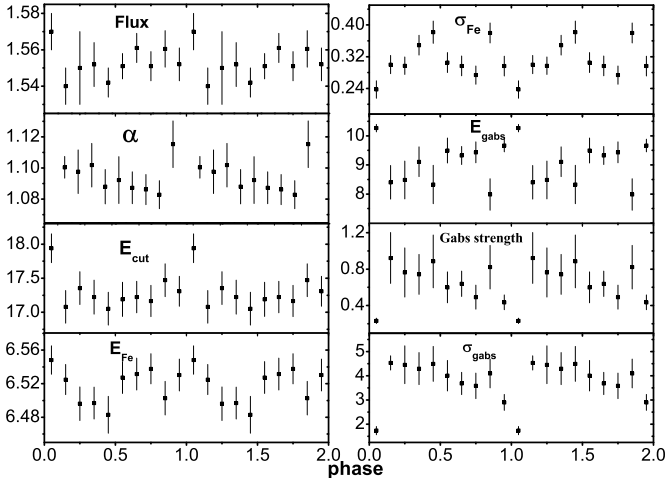


Figure 12. Modulation of phase-resolved parameters using Obs I of NuSTAR represented by ID 80701320002 observed on 59456.0389 MJD. Flux is in the order of $10^{-8} \text{ erg cm}^{-2} \text{ s}^{-1}$. E_{cut} , E_{Fe} and E_{gabs} are measured in keV.

keV attaining its minimum in (0-0.1) and maximum in (0.1-0.2) phase interval. From figure 12, we can see that the width (σ_{gabs}) and strength of Gabs line shows negative correlation with Gabs line energy (E_{gabs}). The absorption feature at ~ 10 keV has been observed in all of the phases.

DISCUSSION

In this paper, we have presented the timing and spectral analysis of EXO 2030+375 using two NuSTAR observations, one lying on the peak and the other along the decaying phase of the outburst. In addition to it, we considered 37 NICER observations almost covering the entire period during its 2021 giant (type II) outburst. The source luminosity has been observed to be as high as $\sim 9.49 \times 10^{37} \text{ erg s}^{-1}$ in (3.0-79.0) keV energy range with NuSTAR observation taken on 59456 MJD. However, in the soft energy band (0.7-10.0 keV), the maximum luminosity of the source has been observed to be $\sim 4.23 \times 10^{37} \text{ erg s}^{-1}$ by considering NICER observations. The pulse profile has been observed to evolve with luminosity revealing a transition from pencil-beam geometry to fan-beam nature on approaching maximum luminosity limit. The luminosity-resolved pulse profiles correspond to observations at different points of time. Therefore, the variability in the nature of the pulse profiles represented in figure 5 reveals the time evolution of pulse profiles. We found the spinning up of the pulsar during the outburst until it reached an equilibrium phase. In case of an accreting neutron star, the pulse period variation is related to the interaction between magnetosphere of the neutron star and the accreting gas. According to the standard theory, the condition for accretion is that the radius of the magnetosphere of the neutron star should be lesser than the corotation radius (Henrichs 1983). The matter falls into the stellar surface if the rotational velocity of the accreting matter is less than the Keplerian velocity. However, if the magnetospheric radius is greater than or equal to the corotation radius, the centrifugal barrier emerges and the matter is thrown out beyond the capture radius by the magnetic field. The neutron star then enters the propeller regime which results in a distinct spin down evolution in its pulse period. The energy dependence of the pulse profiles is relevant from figure

2. The energy-resolved pulse profiles are found to attain distinct variabilities transforming from a fan-beam to a pencil-beam nature significantly observed above ~ 30 keV suggesting a transition in the accretion regime of the pulsar from sub-critical to the super-critical regime.

In our study with NICER observations, when the source luminosity was as low as $\sim 3.36 \times 10^{36} \text{ erg s}^{-1}$, it is found to exhibit a pulse period of $\sim 41.195 \text{ s}$ on 59544 MJD. The *Fermi*/GBM data shows that the source attained a maximum spin frequency i.e., minimum pulse period of $\sim 41.194 \text{ s}$ on 59553 MJD. This can be interpreted as an equilibrium period after which the source has been found to experience a spin down for a short span of time until 59559 MJD. However, the *Fermi*/GBM data reveals that the source started spinning up again after 59559 MJD. Careful analysis of the archival data and previously reported informations have been used to produce substantial results. The hustle related to the negative residuals associated with the NuSTAR observations adds more complexity to it. Such prominent observations and suitably fitted spectra leads us to a temptation of quoting the feature observed at ~ 10 keV as a cyclotron line. Further, this feature was also distinctly observed in the phase resolved spectra corresponding to all the phases adding more weightage to this fact. However, the theories predicted in the past (Klochkov et al. 2008) have led to uncertain aspects about it. Klochkov et al. (2008) also considered relation between CRSF energy and spectral cutoff energy (refer fig 9 of Coburn et al. (2002)) questioning the declaration of 10 keV feature as CRSF to be unusual. This 10 keV feature that has been found in many pulsars is unclear which can be due to drawback of semi phenomenological models used in spectral fitting (Coburn et al. 2002). For simplicity, if we interpret the feature ~ 10.12 keV as a cyclotron line (Wilson et al. 2008), then the magnetic field associated with the system can be computed using the expression: $E_{\text{cyc}} = 11.6 B_{12} \times (1+z)^{-1} \text{ keV}$ where B_{12} represents the magnetic field strength in units of 10^{12} G and $z \sim 0.3$ is the gravitational redshift in the scattering region corresponding to standard neutron star parameters. Assuming a distance of 7.1 kpc, the magnetic field associated with the system was found out to be $\sim 1.13 \times 10^{12} \text{ G}$. This is in accordance with the typical field of a neutron star. Interestingly, the critical luminosity of the system was found to show coincidence with the transitional luminosity observed in the pulse profile and photon index features. Amidst all the twists and turns, we have made use of NICER observations for deeper understanding of the source. Due to limitations in the feasibility of energy ranges in NICER, we noticed the presence of an iron emission line ~ 6.6 keV in the X-ray continuum observed in the (0.7 -10) keV energy range. However, no absorption features were observed in the said energy band. A very interesting character of the Iron emission line was observed in due course of our analysis. The width of the line was found to diminish with luminosity which disappeared as the luminosity approached to the order of $\sim 10^{36} \text{ erg s}^{-1}$. The spectral analysis of the NICER observations, revealed the dependence of photon index with luminosity. A bi-modal behaviour in the variation of the power-law photon index with increasing luminosity is clearly observed from figure 10. At low luminosities, the power-law photon index is found to be anti-correlated with the luminosity of the source which validates the fact that the spectral shape depends on the rate of mass accretion. Negative correlation between the power-law photon index and luminosity reflects the spectrum to be relatively soft at low luminosities. However, a positive correlation between powerlaw photon index and luminosity was seen at higher luminosities. This may be a result of two different accretion regimes (Reig & Nespoli 2013) defined by a certain critical luminosity (Becker et al. 2012). In the sub-critical accretion regime, an

increase in luminosity leads to an increase in the height of emission zone in accretion column to approach towards the object's surface. However, in the super-critical accretion regime, the emission zone shifts up in the accretion column. The Comptonization of photons takes place between the radiative shock and the sinking zone of the object. This region is small in supercritical state while its height increases with increasing luminosity (Becker *et al.* 2012). The region between the radiative shock and the neutron star is linked with a balanced rate of diffusion and advection which lowers the velocity of the comptonising electrons. As a result, the Comptonization process is not strong enough to provide an adequate amount of energy to the photons to excite them which leads to softness of the photons with increasing luminosity. So, the positive correlation of photon index with luminosity is established. However, in the sub-critical regime, the height of the emission region is found to deplete with increasing luminosity. This depletion in the size of the sinking region, causes an increase in the optical depth leading to an increase in hardness of photons (Reig & Nespoli 2013). This agrees with the hardening of photons with increase in luminosity. The pulse fraction bears an overall anti-correlation with luminosity. The frequency derivative is positively correlated with the luminosity of the system. The data points fitted using the POWER-LAW model is in accordance with theoretical predictions. The source under consideration has been known to undergo frequent astronomical activities and will hopefully be explored further with more concrete evidences related to the features of the source.

ACKNOWLEDGEMENT

The publicly available data of the pulsar provided by High Energy Astrophysics Science Archive Research Center (HEASARC) Online Service data archive has been used for our study. The *Fermi*/GBM and *Swift*/BAT data used in the research is provided by Fermi-GAPP and Swift/BAT team respectively. We would like to thank anonymous reviewer for his/her valuable comments and suggestions which helped us in improving the manuscript both in quality and quantity. RT would like to acknowledge CSIR/NET for a research grant 09/0285(11279)/2021-EMR-I. Authors are thankful to IUCAA Center for Astronomy Research and Development (ICARD), Physics Dept, NBU for extending research facilities.

DATA AVAILABILITY

The observational data used in this study can be accessed from the HEASARC data archive and is publicly available for carrying out research work.

REFERENCES

- Arnaud, K. A. 1996, in *Astronomical Data Analysis Software and Systems* V, eds. G. H. Jacoby, & J. Barnes, ASP Conf. Ser., 101, 17
- Barthelmy, S. D., Barbier, L. M., Cummings, J. R., et al. 2005, *Space Science Reviews*, 120, 143
- Becker P. A. et al., 2012, *A & A*, 544, A123
- Boldin P. A., Tsygankov S. S., Lutovinov A. A., 2013, *Astrophys. Let.*, 39,375
- Coburn, W., Heindl, W. A., Rothschild, R. E., et al. 2002, *ApJ*, 580, 394
- Coe, M. J., Payne, B. J., Longmore, A., & Hanson, C. G. 1988, *MNRAS*, 232, 865
- Corbet R. H. D., Levine A. M. 2006, *ATel*, 843
- Davies S. R., 1990, *MNRAS*, 244, 93
- Epili P., Naik S., Jaisawal G. K., Gupta S., 2017, *MNRAS*, 472, 3455
- Ferrigno C., Pjanka P., Bozzo E., Klochkov D., Ducci L., Zdziarski A. A., 2016, *A & A*, 593, A105
- Fürst F., Grinberg V., Tomsick J.A., et al., 2016, *ApJ* 828, 34
- Fürst F. et al., 2017, *A & A*, 606, 89
- Gendreau K. C., et al., 2016, in *Space Telescopes and Instrumentation 2016: Ultraviolet to Gamma Ray*, p. 99051H, doi:10.1117/12.2231304
- Ghosh P., Lamb F. K., 1979, *ApJ*, 234, 296
- Harrison F.A. et al. 2013, *ApJ*, 770, 103
- Henrichs H.F., 1983, in Lewin W., van den Heuvel E., eds, *Accretion-driven Stellar X-ray Sources*. Cambridge Univ. Press, Cambridge, p. 402
- Jaisawal G. K., Naik S., Epili P., 2016, *MNRAS*, 457, 2749
- Jaisawal G. K., et al. 2019, *ApJ*, 885, 18
- Ji, L., Doroshenko, V., Santangelo, A., Güngör, C., Zhang, S., Ducci, L., Zhang, S.N., Ge, M.Y., Qu, L.J., Chen, Y.P. and Bu, Q.C., 2020. Timing analysis of 2S 1417 624 observed with NICER and Insight-HXMT. *Monthly Notices of the Royal Astronomical Society*, 491(2), pp.1851-1856.
- Klochkov, D., Horns, D., Santangelo, A., Staubert, R., Segreto, A., Ferrigno, C., Kretschmar, P., Kreykenbohm, I., La Barbera, A., Masetti, N. and McCollough, M., 2007. INTEGRAL and Swift observations of EXO 2030+ 375 during a giant outburst. *Astronomy & Astrophysics*, 464(3), pp.L45-L48.
- Klochkov D., Santangelo A., Staubert R., Ferrigno C., 2008, *A & A*, 491, 833
- Kretschmar P., et al., 2016, *ATel*, 9485
- Krimm H., Barthelmy S., Gehrels N., Markwardt C., Palmer D., Sanwal D., Tueller J., 2006, *ATel*, 861
- Krimm, H. A., Holland, S. T., Corbet, R. H. D., et al. 2013, *ApJS*, 209, 14
- Larsson S., 1996, *A & AS*, 117, 197
- Meegan, C., Lichti, G., Bhat, P. N., et al. 2009, *The Astrophysical Journal*, 702, 791
- Mihara, T. 1995, Ph.D. thesis, Riken, Tokyo
- Motch C., Janot-Pacheco E., 1987, *A & A*, 182, L55
- Naik S., Maitra C., Jaisawal G. K., Paul B., 2013, *ApJ*, 764, 158
- Naik S., Jaisawal G. K., 2015, *RAA*, 15, 537
- Okazaki A. T., Negueruela I., 2001, *A & A*, 377, 161
- Parmar, A. N., White, N. E., Stella, L., Izzo, C., & Ferri, P. 1989, *ApJ*, 338, 359
- Paul B., Naik S., 2011, *BASI*, 39, 429
- Reig P., 2011, *Ap & SS*, 332, 1
- Reig, P. & Nespoli, E., 2013, *A & A*, 332, 1-29
- Remillard, R. A., Loewenstein, M., Steiner, J. F., et al. 2021, *arXiv e-prints*, arXiv:2105.09901. <https://arxiv.org/abs/2105.09901>
- Serim, M. M. et. al., 2022, *MNRAS*, 510, 1438–1449
- Shaw S. E., Hill A. B., Kuulkers E., Brandt S., Chenevez J., Kretschmar P., 2009, *MNRAS*, 393, 419
- Stella L., White N.E., Rosner R., 1986, *ApJ* 308 669
- Tanaka, Y. 1986, in *Radiation Hydrodynamics in Stars and Compact Objects*, Mihalas, D. & Winkler, K.H. (eds.), (Springer:New York, Heidelberg), p.198
- Tauris, T.M. and Van Den Heuvel, E.P.J., 2006. Formation and evolution of compact stellar X-ray sources. *Compact stellar X-ray sources*, 39, pp.623-665.
- Wilson C. A., Finger M. H., Coe M. J., Laycock S., Fabregat J., 2002, *ApJ*, 570, 287
- Wilson C. A., Fabregat J., Coburn W., 2005, *ApJ*, 620, L99
- Wilson C. A., Finger M. H., Camero-Arranz A., 2008, *ApJ*, 678, 1263-1272
- Wilson-Hodge C. A. et al., 2018, *ApJ*, 863, 9

This paper has been typeset from a \LaTeX file prepared by the author.